



# Molecular-level insights on NIR-driven photocatalytic H<sub>2</sub> generation with ultrathin porous S-doped g-C<sub>3</sub>N<sub>4</sub> nanosheets

Xiaojie Wu, Di Li, Bifu Luo, Biyi Chen, Yuanyong Huang, Tingting Yu, Nanjun Shen, Longhua Li, Weidong Shi<sup>\*</sup>

School of Chemistry and Chemical Engineering, Jiangsu University, 301 Xuefu Road, Zhenjiang 212013, Jiangsu, China

## ARTICLE INFO

### Keywords:

Near infrared driven photocatalytic  
Sulfur doping  
Intermediate band gap  
Ultrathin porous  
Carbon nitride nanosheets

## ABSTRACT

Unraveling how mid-gap state energy level of graphitic carbon nitride (g-C<sub>3</sub>N<sub>4</sub>) promote near-infrared (NIR) driven photochemical energy conversion at the molecular level remains a grand challenge. Here, we report a series of S double-site-doped ultrathin g-C<sub>3</sub>N<sub>4</sub> nanosheets (SUCN) with adjustable intermediate band gap benefits from light response over NIR region. The SUCN produced after optimizing S double-site doping can effectively generate hydrogen (H<sub>2</sub>) under NIR-light irradiation. The highest H<sub>2</sub> generation rate achieved was respectively 9.35 and 17.46 μmol g<sup>-1</sup> h<sup>-1</sup> under λ = 765 and λ > 800 nm, which is firstly expended photocatalytic activity of S-doped g-C<sub>3</sub>N<sub>4</sub> to NIR region beyond λ > 765 nm. We proposed a molecular-level method, i.e., the localized oxidation state of proton acceptor triethanolamine (TEOA) in the mid-gap state to ensure the NIR-driven H<sub>2</sub> generating behavior.

## 1. Introduction

Photocatalytic hydrogen evolution (PHE) using semiconductors and solar energy is a promising technology for the production of clean and renewable chemical fuels [1]. Of the various photocatalysts that have been reported for PHE, crystalline graphitic carbon nitride (g-C<sub>3</sub>N<sub>4</sub>) has garnered much attention as metal-free and high abundance [2]. Unfortunately, inadequate light utilization and severe photocarrier recombination are generally considered as typical constraints of g-C<sub>3</sub>N<sub>4</sub> [3]. However, only a few portions of single-component g-C<sub>3</sub>N<sub>4</sub> could meet expectations. [4]. Therefore, producing single-component g-C<sub>3</sub>N<sub>4</sub> with high PHE performance under NIR light are capable as one of valuable challenges [5].

Recently, the covalent heteroatom-doping (N, C, B, S, etc.) photocatalysis technology coupled with g-C<sub>3</sub>N<sub>4</sub> has attracted extensive research interest due to its expanding light response and increasing charge separation rate [6–11]. Covalent heteroatom-doping can be described as electron acceptors for photocarrier. Especially, the introduction of atom-sized S has been shown to not only maximize the activity of the C atom adjacent to the heteroatom, but also adjust the interlayer distances of g-C<sub>3</sub>N<sub>4</sub> [12,13]. Moreover, the half-filled 3p orbital of S could induce an intermediate band gap in the intermediate band gap of g-C<sub>3</sub>N<sub>4</sub> to accommodate more long-wavelength excited

charge carriers and promote the excitons separation [14,15]. However, although S-doping has made an important contribution to the local electric neutral state in the heptazine-conjugated skeleton, the mid-gap state energy level caused by the doping position was seldom investigated [16]. Controlling the S-doping sites in the heptazine-conjugated skeleton and elucidating the mechanism of mid-gap state energy level is considered to be a crucial challenge for circumventing NIR-energy conversion limitation [17,18].

Herein, we demonstrate the synthesis of S double-site-doped ultrathin g-C<sub>3</sub>N<sub>4</sub> nanosheets (SUCN) via the in-situ synthesis strategy in the bottom-up acidification process. Compared to a trace amount of H<sub>2</sub> evolution by bulk g-C<sub>3</sub>N<sub>4</sub>, the optimum H<sub>2</sub> generation rate of SUCN reached 161.32 μmol h<sup>-1</sup> under the Vis light radiation. Unexpectedly, the optimum specimen also showed evolution rate of H<sub>2</sub> (9.35 and 17.46 μmol g<sup>-1</sup> h<sup>-1</sup>) under λ = 765 and λ > 800 nm, respectively. Urbach calculations confirmed that the SUCN were formed intermediate energy level positions between forbidden band. To get clear proofs of NIR-driven H<sub>2</sub> evolution mechanism, the localized oxidation state of triethanolamine (TEOA) under the NIR irradiation was carried out. The results indicate that NIR-driven H<sub>2</sub> generation is driven by excited electrons in the mid-gap state.

<sup>\*</sup> Corresponding author.

E-mail address: [swd1978@ujs.edu.cn](mailto:swd1978@ujs.edu.cn) (W. Shi).

<https://doi.org/10.1016/j.apcatb.2022.122292>

Received 25 October 2022; Received in revised form 2 December 2022; Accepted 11 December 2022

Available online 13 December 2022

0926-3373/© 2022 Published by Elsevier B.V.

## 2. Experimental section

### 2.1. Materials

Melamine (MA,  $\geq 99\%$ ), trithiocyanuric acid (TTCA,  $\geq 99\%$ ), acetonitrile (ACN,  $\geq 99\%$ ),  $\text{H}_2\text{SO}_4$  ( $\geq 99\%$ ), ethyl alcohol (EtOH,  $\geq 99\%$ ),  $\text{Na}_2\text{SO}_4$  ( $\geq 99\%$ ), triethanolamine (TEOA) and  $\text{H}_2\text{PtCl}_6$  were purchased from Sinopharm Chemical Reagent Co., Ltd and all reagents employed in this study without further purification. Deionized water throughout the whole experimental process was purified by an ultrapure water system supplied by RSJ Co., Ltd.

### 2.2. Synthesis of photocatalysts

The SUCN was synthesized via a simple method with some optimizations. Briefly, 400 mg of MA, a certain amount of TTCA (90, 180, 270, 360, and 450 mg) and 3 mL  $\text{H}_2\text{SO}_4$  was added in 30 mL of ACN aqueous solution and stirred for 4 h. Then, transferred the suspension to the 50 mL Teflon-lined autoclave and heated at  $100^\circ\text{C}$  for 24 h. The obtained precursor washed with excess EtOH and  $\text{H}_2\text{O}$  and dried under vacuum at  $60^\circ\text{C}$ . After grounding into powder, SUCN was obtained by heated in Ar atmosphere at  $550^\circ\text{C}$  for 4 h with a ramping rate of  $7^\circ\text{C min}^{-1}$ . The SUCN was labeled x-SUCN ( $x = 0.09, 0.18, 0.27, 0.36$ , and  $0.45$  g), where  $x$  represented the quality of TTCA added into the precursor.

Meanwhile, a sample of  $\text{g-C}_3\text{N}_4$  nanosheets was prepared similarly, except that 360 mg TTCA or 3 mL  $\text{H}_2\text{SO}_4$  was not added [19,20]. The S doping  $\text{g-C}_3\text{N}_4$  was labeled SCN and ultrathin  $\text{g-C}_3\text{N}_4$  was labeled UCN [21].

### 2.3. Physicochemical characterization

X-ray diffraction (XRD) patterns were performed on a D/MAX-2500 diffractometer with Cu K $\alpha$  radiation ( $\lambda = 1.54178 \text{ \AA}$ ) and radiation in the  $2\theta$  domain of  $10.0\text{--}80^\circ$  ( $7.0^\circ/\text{min}$ ). FT-IR was collected on the Nexus 470 (Thermo Electron Corporation). SEM was examined on an S-4800 field-emission scanning electron microscope (Hitachi, Japan). Transmission electron microscopy (TEM) was obtained using the Tecnai G2 F30 S-TWIN. Elemental mapping pattern was recorded by an energy-dispersive/X-ray spectrometer (EDS) attached to the TEM instrument. X-ray photoelectron spectroscopy (XPS) measurements were implemented by the Thermo Scientific ESCALAB 250Xi. UV-visible spectroscopy (UV-Vis) was characterized by a Shimadzu UV-2450 spectrometer. Photoluminescence (PL) spectra was operated on the Quanta Master™ 40 fluorophotometer spectrometer. The solid-state  $^{13}\text{C}$  nuclear magnetic resonance ( $^{13}\text{C}$  NMR) spectra was investigated on a Switzerland Bruker model 600 M spectrometer by Shiyanjia Lab (www.shiyanjia.com). Time-resolved photoluminescence spectra was recorded on a Quanta Master & Time Master Spectro-fluorometer. All photoelectrochemical measurements were measured by using an electrochemical workstation (CHI-852 C, Shanghai Chenhua Limited, China) with a conventional standard three-electrode cell. All photoelectrochemical measurements were carried out in a CHI-852 C electrochemical workstation.

### 2.4. Photocatalytic reaction

Photocatalytic activities were evaluated in quartz reactor by dispersing the catalysts (20 mg) in a 50 mL aqueous TEOA solutions (10 vol%). The reaction mixture was irradiated by a 300 W xenon lamp ( $100 \text{ mW cm}^{-2}$ ) after loading on 2 wt% Pt with  $\text{H}_2\text{PtCl}_6 \cdot 6 \text{ H}_2\text{O}$  aqueous solution. The temperature was maintained at  $5^\circ\text{C}$  by a flow of cooling water throughout the photocatalytic reaction process. The amount of  $\text{H}_2$  generation rate was evaluated on a GC-7920 gas chromatograph every hour. Besides, the cycle test and the apparent quantum efficiency (AQE) of photocatalytic  $\text{H}_2$  production rate was carried out under the same conditions.

### 2.5. Computational details

All the spin-polarized density functional theory (DFT) were consummated using the Vienna ab initio simulation package (VASP). In order to get accurate results, the Perdew-Burke-Ernzerhof (PBE) exchange-correlation functional within a generalized gradient approximation and the projector augmented-wave potential were calculated. The heteroatoms of S were embedded in a  $2 \times 2 \times 1$  octahedron the bulk  $\text{g-C}_3\text{N}_4$  with a vacuum of  $20 \text{ \AA}$ . The K point division  $1 \times 1 \times 1$  was sampled in a  $3 \times 3 \times 1$  Monkhorst-Pack grid to structural optimization and self-consistent calculation. The energy cutoff was set to 550 eV for the plane-wave expansion.

## 3. Results and discussion

### 3.1. Morphological characterization

The possible polymerization process for incorporating off S building blocks from TTCA into the heptazine-conjugated skeleton of  $\text{g-C}_3\text{N}_4$  structure was fabricated (Fig. 1. a). The thiol group of thiocyanuric acid reacts with the hydroxyl group in water to form a thioether bond. Concentrated sulfuric acid dissolved in acetonitrile oxidizes the thioether bond to form matte salt prepolymer. At the same time, as Brønsted acid, concentrated sulfuric acid breaks the hydrogen bond between melamine plates. The XRD patterns confirmed the similar feature of SUCN. Moreover, the (002) peak in Fig. S1. (a) provided a significant reduction in the interlayer distance of other contrast samples [22]. The XRD patterns of bulk  $\text{g-C}_3\text{N}_4$  in Fig. S1. (a) showed two peaks at  $13.2^\circ$  and  $27.1^\circ$  that was attributed to crystal face characteristics of interlayer repeating structural and the in-plane stacking of aromatic segments, respectively. Although the x-SUCN showed similar crystal structures to  $\text{g-C}_3\text{N}_4$ , the width of (002) peak shape became broadens and up-shifted. This result indicated that a synergy effect of S double-site-doped and acid etching reduced the crystallinity and destroyed the orderly arrangement of  $\text{g-C}_3\text{N}_4$  [16].

The crystal phase and microstructure of  $\text{g-C}_3\text{N}_4$  and S-doping  $\text{g-C}_3\text{N}_4$ , were studied by SEM and TEM. As displayed in Fig. 2. (a-b), the  $\text{g-C}_3\text{N}_4$  showed a representative stacked structure, while the 0.36-SUCN displayed porous multilayer two-dimension nanosheets with irregular nanopores (5–25 nm), which were consistent with Fig. S1. (b-d) in the Supporting Information. All the elements (i.e., N, C, and S) were homogeneous distributed on the 0.36-SUCN in Fig. 2. (c-f), suggesting that S has been incorporated into the heptazine-conjugated skeleton [23]. The AFM in Fig. 2. (g) demonstrated that 0.36-SUCN was the laminar structure with ultrathin thickness. The stochastically measured thickness of the nanosheets was 1.1 nm in Fig. 2. (h). The  $\text{N}_2$  sorption isotherms of 0.36-SUCN and  $\text{g-C}_3\text{N}_4$  exhibited a typical type-IV curve with a representative  $\text{H}_3$ -type hysteresis loop in Fig. 2. (i) [24]. The specific surface area (SSA) of 0.36-SUCN based on BET was calculated to  $38.21 \text{ m}^2 \text{ g}^{-1}$  with a nearly 3-fold increase than that  $\text{g-C}_3\text{N}_4$  ( $12.96 \text{ m}^2 \text{ g}^{-1}$ ). As exhibited in Fig. S1. (f), the pore volume obtained from the pore size distribution curve of 0.36-SUCN and bulk  $\text{g-C}_3\text{N}_4$  were  $0.26 \text{ cm}^3 \text{ g}^{-1}$  and  $0.14 \text{ cm}^3 \text{ g}^{-1}$ , respectively. Thus, the highly micro mesopore structure of 0.36-SUCN not only shorten the diffusion path of photoexcited carriers, but also supplied a larger surface area for photocatalytic active sites [21,25].

### 3.2. Structure characterization and optical/electronic properties

Molecular functional groups of a series of photocatalysts were collected by FT-IR [26]. The broad absorption characteristic peaks located in  $1100\text{--}1650 \text{ cm}^{-1}$  were assigned to the C-N skeletal vibration in Fig. 3. (a) & S1. (b) [3]. The FTIR spectra of the S-doped  $\text{g-C}_3\text{N}_4$  indicated only the vibration peak relatively changes at  $808 \text{ cm}^{-1}$  owing to the low S content [27]. The XPS S 2p spectra (Fig. 3. (b)) to further confirm the presence of sulfur in 0.36-SUCN material. The signal

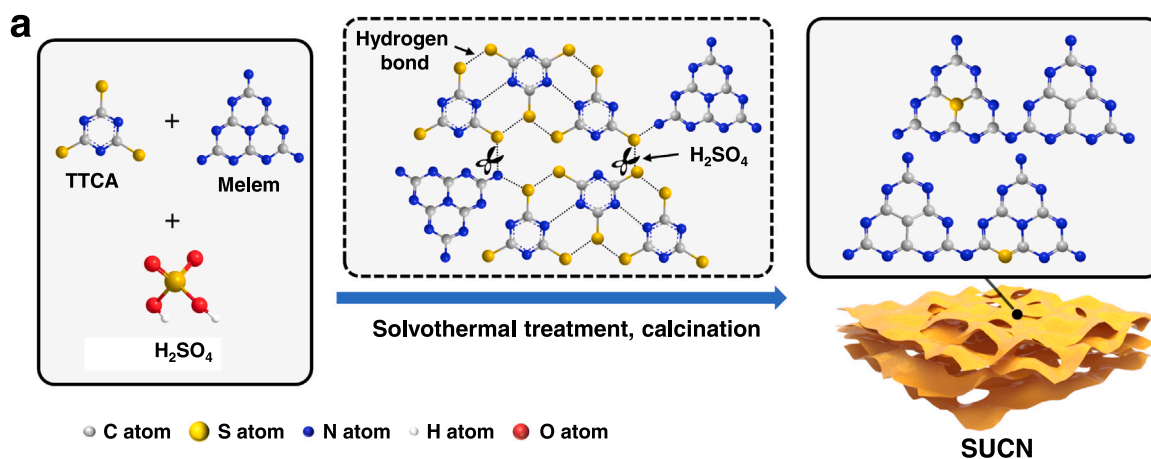
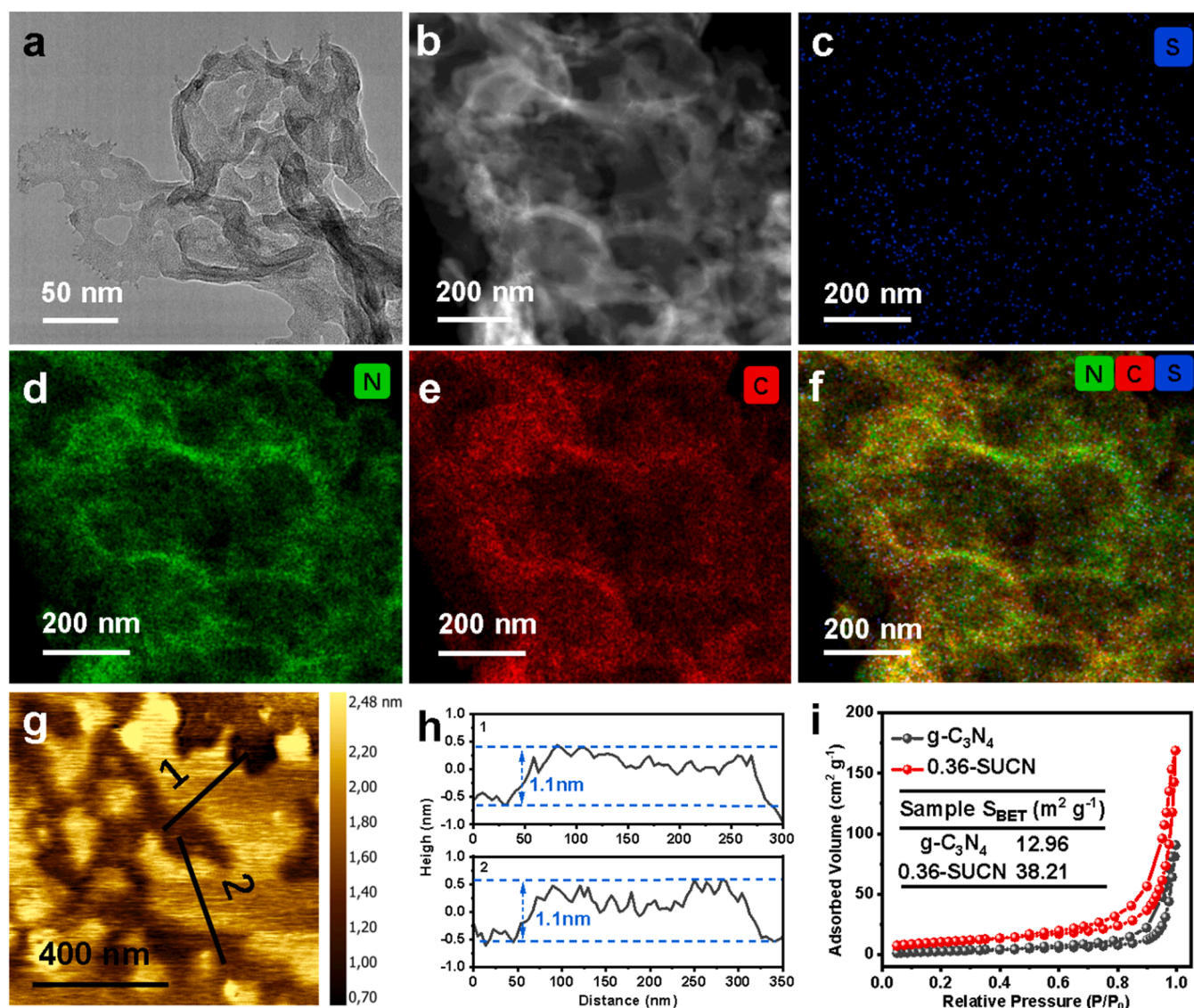
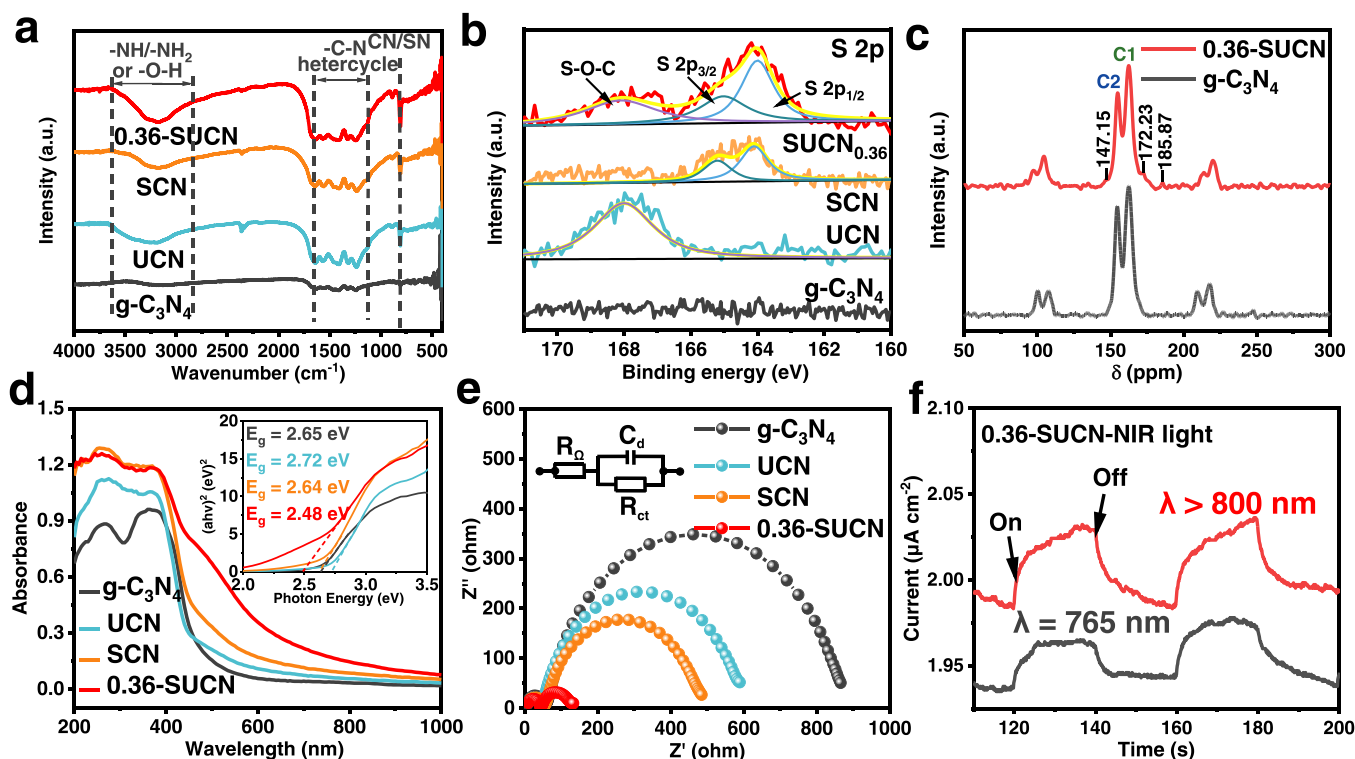


Fig. 1. (a) Schematic representation for the SUCN synthesis process.

Fig. 2. (a) TEM image of 0.36-SUCN (b) the inset of TEM image showed the corresponding region for mapping; (c-f) EDS mapping of 0.36-SUCN. (g) AFM image and (h) corresponding height profiles along the white line in d of 0.36-SUCN. (i) N<sub>2</sub> sorption isotherms of g-C<sub>3</sub>N<sub>4</sub> and 0.36-SUCN.





**Fig. 3.** (a) The FTIR spectra. (b) High-resolution S 2p XPS spectrum. (c) The solid-state  $^{13}\text{C}$  NMR spectra. (d) UV-visible plots. Inset: the relationship between Kubelka-Munk function and photon energy. (e) Impedance spectra. Inset: equivalent circuit impedance model. (f) Transient photocurrent curves under NIR light.

intensity of S 2p was not strong (Fig. S3 (a)) due to the low doping content. The binding energy of S 2p was deconvoluted into four peaks, which were located at 168.1, 165.0, and 164.0 eV. The peaks at 164.0 and 165.0 eV were assigned to the S 2 $P_{1/2}$  and S 2 $P_{3/2}$  bonds, while another weak peak at 168.1 eV were attributed to the high-valent S species formed during calcination [28]. Moreover, the variations of atomic ratios between g- $\text{C}_3\text{N}_4$  and 0.36-SUCN (Table S1) were also demonstrated by XPS. The N/C atomic ratio of 0.36-SUCN decreased from 1.293 to 1.229. Additionally, the N/C and S/C ratios of 0.36-SUCN is much lower, indicating the existence of nitrogen defects [29]. Simultaneously, the S element can act as a photoelectron capturing site, which greatly reduces the backward charge recombination, and ultimately benefits the photo-redox process [30].

Moreover, the chemical structure of 0.36-SUCN was further investigated via the solid-state  $^{13}\text{C}$  NMR in Fig. 3. (c) & S3. (d). Typical,  $^{13}\text{C}$  NMR peaks of the bulk g- $\text{C}_3\text{N}_4$  (151 MHz, none) were 217.68, 209.48, 162.61, 154.60, 107.65 and 100.28. In contrast, 0.36-SUCN exhibited three distinct peaks [ $^{13}\text{C}$  NMR (151 MHz, none)  $\delta$  220.03, 213.83, 185.87, 172.23, 162.58, 154.87, 147.15, 104.47, and 97.34]. The two weak peaks located at 185.87 and 147.15 ppm were probably attributed to the chemical shifts of the C3 atom ( $\text{CN}_2=\text{S}$ ) and C4 atom ( $\text{CN}_2=\text{N}$ ), respectively in Fig. S4. Another weak peak at 172.23 ppm was probably related to C5 atoms of the S- $\text{CN}_2$  group. The UV-Vis DRS was implemented the optical characteristics of g- $\text{C}_3\text{N}_4$  and other contrast samples in Fig. 3. (d) & S3. (e). The optical absorption of 0.36-SUCN was greatly enhanced in Fig. S3 (e), indicating the reduced band gap [31]. As expected, 0.36-SUCN showed an obvious absorption tail over 400–700 nm and extended to the longer wavelength (near 1000 nm). The energy gap ( $E_g$ ) of bulk  $\text{C}_3\text{N}_4$  acquired by the Kubelka-Munk-plot transform function was 2.65 eV [32]. In comparison, the obtained decreasing trend of  $E_g$  valued from 2.65 to 2.48 eV for x-SUCN.

Apart from the suitable  $E_g$ , the relevant energy level matching the redox potential reaction was also a major parameter evaluate the performance of photocatalysts [33]. On the basis of the Mott-Schottky plots in Fig. S5. (a-h), the samples displayed positive slopes, demonstrating the

n-type character of g- $\text{C}_3\text{N}_4$  [34]. The flat band positions ( $E_{\text{FB}}$ ) of the g- $\text{C}_3\text{N}_4$  was  $-1.087$  V (vs Ag/AgCl), while 0.36-SUCN was  $-1.167$  V. Generally, the CB potential of n-type semiconductors was approximately 0.1 V higher than  $E_{\text{FB}}$ , thus the CB of g- $\text{C}_3\text{N}_4$  and 0.36-SUCN were  $-0.987$  eV and  $-1.067$  eV, respectively [35]. The 0.36-SUCN showed a fast and forceful photocurrent response in Fig. S3 (f), and such photocurrent response phenomenon has been acceptive repeated in second on-off cycles. Obviously, the photocurrent response curves of 0.36-SUCN were still clearly observable under NIR illumination in Fig. 3. (f).

The photoinduced excitation splitting properties of the photocatalyst was evaluated by PL emission spectroscopy. As exhibited in Fig. S3. (g), the PL intensity of 0.36-SUCN was lowest [17,18]. In Fig. 3. (e) & S3. (h), the arc radius of the semicircular Nyquist curve from electrochemical impedance spectroscopy (EIS) decreased gradually. This was attributed to the effective shuttle from the electrode to electrolyte and the rapid transfer of interfacial charge on a hydrophilic surface. The lowest EIS of 0.36-SUCN indicated that the ultrathin layer morphology and S-doping in the carbon nitride framework can greatly enhance charge transport (Fig. S3. (h)). Besides, the average fluorescence lifetimes are 3.834 and 2.223 ns for bulk g- $\text{C}_3\text{N}_4$  and 0.36-SUCN (the detailed information is listed in Fig. S3. (i) & Table S2, which was consistent with our assumption. The rapid and uniform photocurrent response curves (Fig. S5. (i)) demonstrated that the x-SUCN possessed a significant higher photocurrent density, confirming the increase of photogenerated charge. Especially, the highest charge separation efficiency of 0.36-SUCN among the x-SUCN was attributed to the ultrathin characteristics and S-doping, which obtains similar trends in EIS and PL measurements.

### 3.3. Photocatalytic performance

The PHE activity of x-SUCN were measured under visible light. As shown in Fig. 4. (a) and S6. (a-b), g- $\text{C}_3\text{N}_4$  showed poor  $\text{H}_2$  generation activity under irradiation of  $\lambda > 420$  nm, which could attribute to the ultra-high electron-hole recombination rate. All-modified

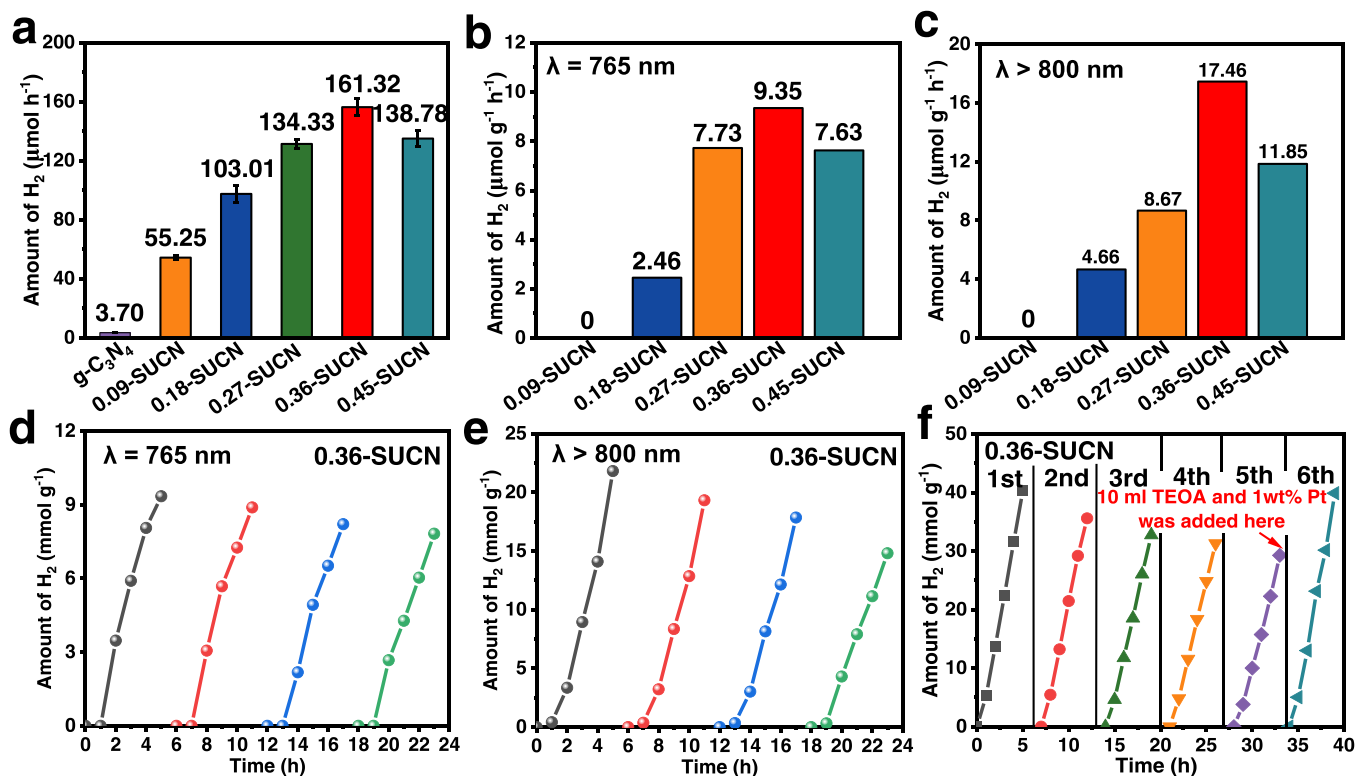


Fig. 4. (a) Photocatalytic H<sub>2</sub> release amount of g-C<sub>3</sub>N<sub>4</sub> and x-SUCN (λ > 420 nm, pH = 7). (b) H<sub>2</sub> generation rates of g-C<sub>3</sub>N<sub>4</sub> and x-SUCN (λ = 765 nm, pH = 7). (c) H<sub>2</sub> generation rates of g-C<sub>3</sub>N<sub>4</sub> and x-SUCN (λ > 800 nm, pH = 7). (d-f) H<sub>2</sub> generation stability estimation of 0.36-SUCN.

photocatalysts exhibited noticeably enhanced activity relative. Surprisingly, 0.36-SUCN showed the highest H<sub>2</sub> generation rate (161.32 mmol h<sup>-1</sup>), which is about 43 times higher than that of g-C<sub>3</sub>N<sub>4</sub> (3.701 mmol h<sup>-1</sup>). The PHE of 0.36-SUCN is significant, and is significantly better than most reported single-element doped and functionalized g-C<sub>3</sub>N<sub>4</sub> in Table S3.

The results of PHE under NIR light irradiation were measured in Fig. 4. (b-c). Obviously, the x-SUCN has enhanced PHE activity under NIR light. The above data demonstrated that S-doping g-C<sub>3</sub>N<sub>4</sub> porous multilayer nanosheet could broaden the light to NIR for the first time. In addition, the stability performance of 0.36-SUCN was collected under the same conditions. Moreover, the PHE of 0.36-SUCN was stable under λ = 765 nm and λ > 800 nm (Fig. 4. (d & e)). As presented in Fig. 4. (f), H<sub>2</sub> evolution reaction of 36-SUCN slightly decreased during the first five cycles, which might be attributed to the consumption of sacrificial agent and cocatalyst. To prove this regard, we added 10 mL TEOA and 1 wt% Pt before the start of the sixth hydrogen production cycle. There was no significant discrimination between the sixth H<sub>2</sub> production cycle and the first H<sub>2</sub> production cycle, suggesting the outstanding stability of 0.36-SUCN under the applied reaction conditions. Moreover, the XRD pattern of the 0.36-SUCN has unchanged after six photocatalytic reactions in Fig. S6. (d). The AQE performances of 0.36-SUCN were measured under a series of wavelength irradiation for exploring wavelength-dependent H<sub>2</sub> evolution. It can be noticed that the AQEs of 0.36-SUCN at 400 and 420 nm were estimated to be about 22.91% and 17.75%, respectively in Fig. S6. (c). Since the band tail absorption was not completely uniform, AQE cannot show a theoretical linear correlation [26].

### 3.4. Theoretical calculations

The PHE of SUCN was closely interrelated to the electronic structure of S in SUCN sites. The values of work function of SUCN and g-C<sub>3</sub>N<sub>4</sub> was calculated by DFT in Fig. 5. (a-b). The results showed that the energy

required for electrons to escape from Fermi level of the SUCN to the vacuum level is much smaller than that of the g-C<sub>3</sub>N<sub>4</sub>. Combined with Fig. 5. (c) & (d), the S 3p hybridizes adjacent atoms presented an electron-rich environment, which was consistent with the electron donor [36]. Densities of states (DOS) was also studied (Fig. S7), considering that the CB and VB of g-C<sub>3</sub>N<sub>4</sub> were both composed of C 2p and N 2p. Thus, the total DOS showed that the band gaps of g-C<sub>3</sub>N<sub>4</sub> was ca. 1.02 eV. In addition, there was no impurity peak between the band gaps. Since the calculation of the exchange correlation function underestimates the energy gap for its own limitations. For SUCN, S 3p participated in the edge hybridization of the valence band, so the CB and VB were composed of C 2p, N 2p and S 3p. As a result, S doping narrowed the band gap and induced a red-shift on the absorption edge. A new impurity peak appeared between the band gaps due to S 3p via the analysis wave state. The appearance of impurity peaks indicated S-doping forms a new energy level between forbidden band and induces n→π\* electronic transition, widened the light absorption range and further enhanced the PHE performance [37].

### 3.5. The mechanism of the photocatalytic reaction

According to Urbach formula, the band edge of the intermediate gap state could be roughly displayed in combination with the constant VB position in Fig. S8. [38,39]. The intermediate state of 0.36-SUCN was close to the CB edge, which shortened the transition distance from the intermediate state to CB edge. Carriers were more easily excited intermediate gap states, and the gap can accommodate electrons excited by longer wavelength photons [40]. Therefore, the CB and VB energy levels could be defined by combination of the CB edges with the E<sub>g</sub> values. The band structures could be inferred as Fig. 6. (a) and S8. (e).

A schematic diagram of the energy band and intermediate gap structure is illustrated in Fig. 6. (b), and the possible process of H<sub>2</sub> release under Vis and NIR light is proposed:

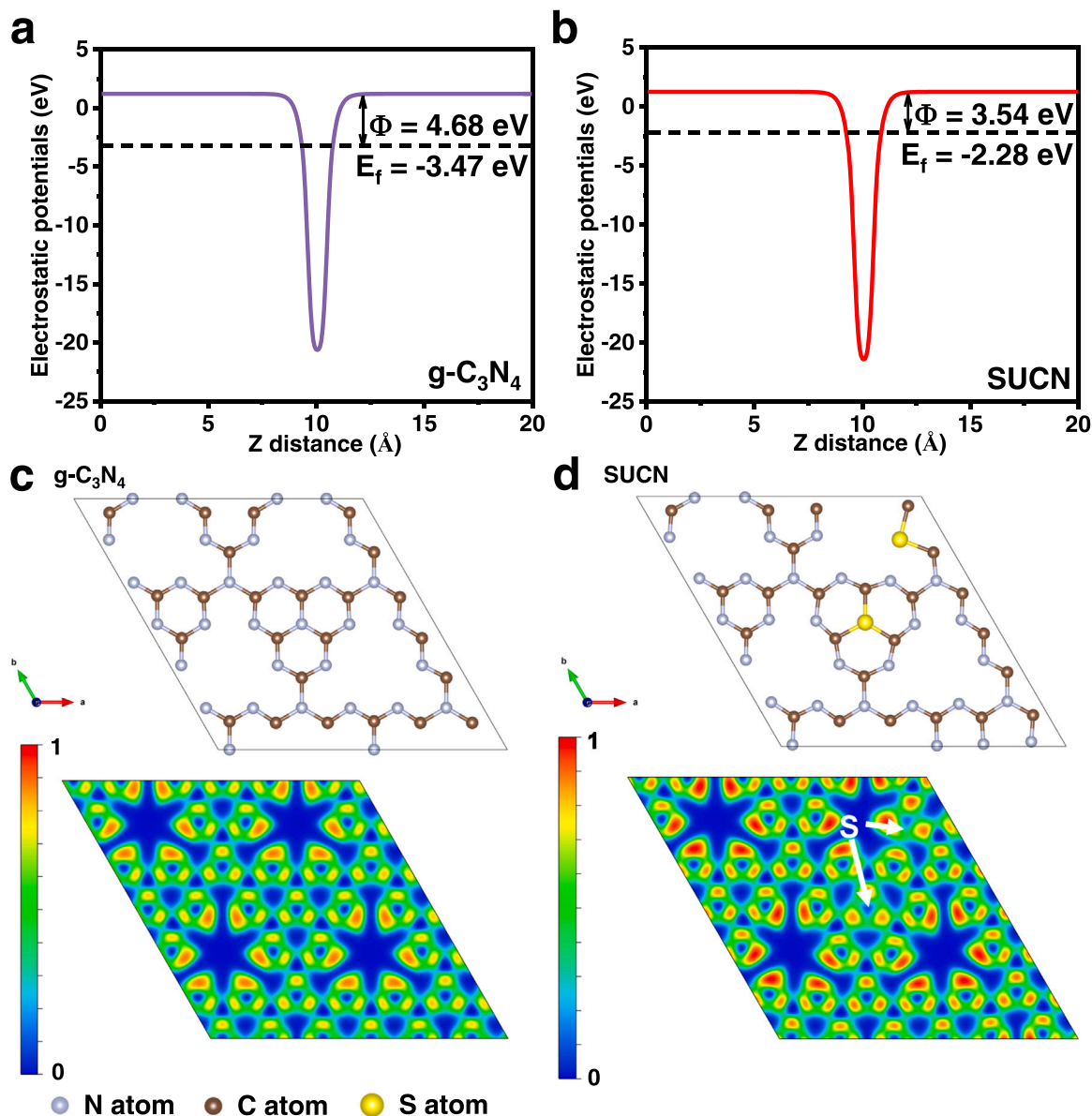
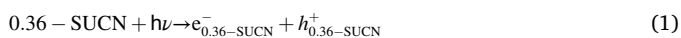


Fig. 5. (a–b) The calculated work functions of g-C<sub>3</sub>N<sub>4</sub> and SUCN. The DFT calculations of the electronic structure of (c) g-C<sub>3</sub>N<sub>4</sub> and (d) SUCN.



The local photooxidation of TEOA during photocatalytic simulation reveals the behavior of H<sub>2</sub> generation driven by the intermediate band gap under the NIR light. The valence band of 0.36-SUCN showed good oxidation behavior, thus an ethyl oxide peak appears under Vis light in Fig. 6. (c). There was almost no difference with TEOA raw material under NIR radiation, because the intermediate band gap is more negative than the valence band of 0.36-SUCN. In view of above experimental data and DFT results, the enhanced PHE activity of SUCN could be ascribed to three points: Firstly, S-doping formed a suitable intermediate band gap between CB and VB to capture long-wavelength excited e<sup>-</sup>. Second, S-doped in the triazine skeleton acted as an electron acceptor could reduce the recombination rate of e<sup>-</sup>-h<sup>+</sup> pairs. Finally, the porous nanosheet structure provided a large specific surface area, which could capture numerous photons and shorten the distance of e<sup>-</sup> transferring from the inside to the surface of the photocatalyst. In addition, porous

structures could provide marginal active sites. Therefore, 0.36-SUCN showed broadband gap absorption, ultra-high visible PHE performance and near-infrared PHE.

#### 4. Conclusions

In conclusion, the S-doped g-C<sub>3</sub>N<sub>4</sub> porous ultrathin material was prepared by a simple heat treatment method. As a result, by doping the triazine skeleton with S element, SUCN could accelerate the separation and transfer of charges, showing excellent H<sub>2</sub> generation activity and high solar energy availability. The PHE of the best sample was 43 times higher than that of the bulk g-C<sub>3</sub>N<sub>4</sub> under  $\lambda > 420$  nm radiation. The S-doped g-C<sub>3</sub>N<sub>4</sub> firstly produced H<sub>2</sub> under NIR light, and its PHE under  $\lambda = 765$  and  $\lambda > 800$  nm radiation was 9.35 and 17.46  $\mu\text{mol g}^{-1} \text{h}^{-1}$ , respectively. The significant relationship between molecular configuration and charge dynamics was demonstrated by DFT calculations. In particular, the PHE performance under NIR radiation was proved by a molecular-level method to be driven by the appropriate intermediate band gap provided by the S-electron acceptor. The precise regulation of element doped g-C<sub>3</sub>N<sub>4</sub> affords a new strategy for greatly improving the

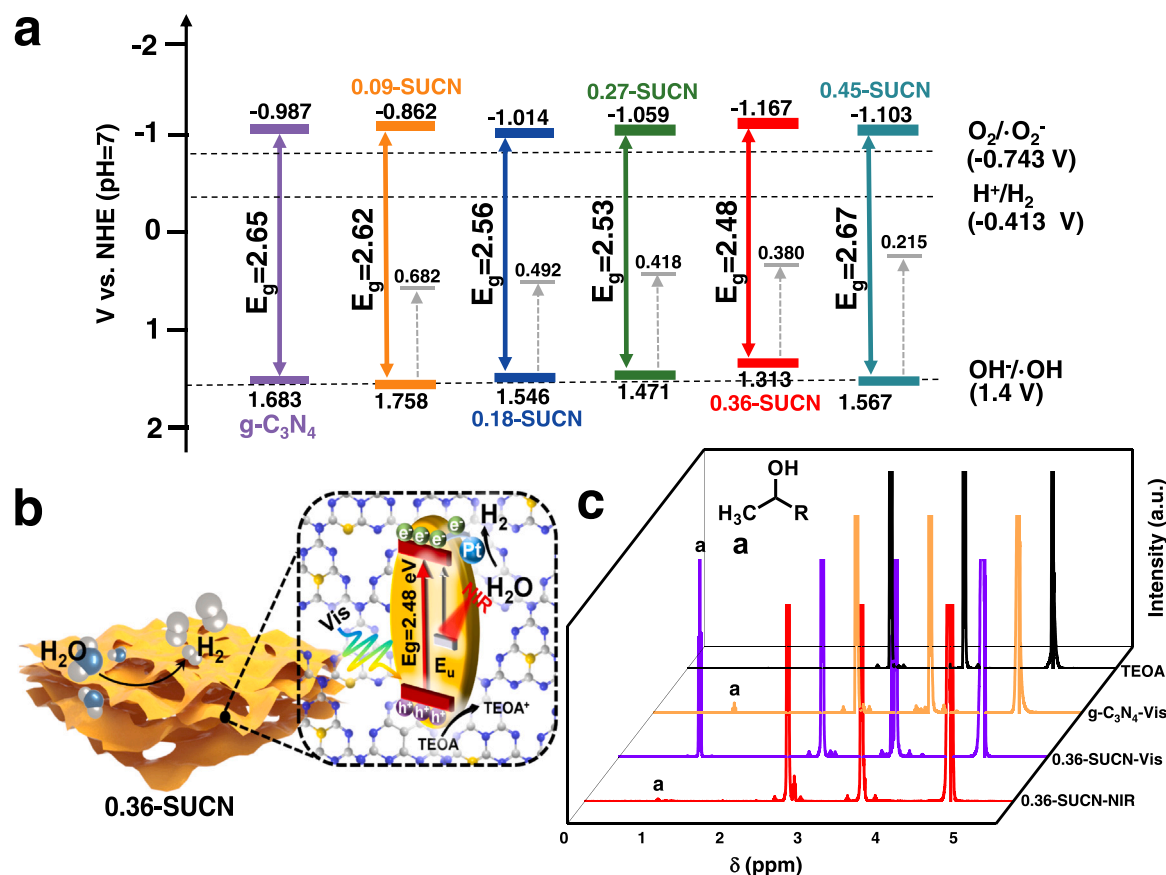


**Fig. 6.** (a) The schematic diagram of the energy band structure. (b) Schematic diagram of  $H_2$  generation through 0.36-SUCN. (c)  $^1H$  NMR of spectroscopy of TEOA after 5 h irradiation in  $D_2O$ .

broad-spectrum solar-energy utilization efficiency.

#### CRediT authorship contribution statement

**Xiaojie Wu:** Conceptualization, Data curation, Formal analysis, Supervision, Validation, Visualization, Writing – review & editing. **Di Li:** Review & editing, Data curation, Supervision. **Bifu Luo:** Data curation, Supervision. **Biyi Chen:** Visualization, Investigation. **Yuanyong Huang:** Validation, Visualization. **Nanjin Shen:** Investigation. **Tingting Yu:** Investigation. **Longhua Li:** Investigation, Supervision. **Weidong Shi:** Funding acquisition, Investigation, Methodology, Project administration.

#### Declaration of Competing Interest

The authors declare that they have no known competing financial interests or personal relationships that could have appeared to influence the work reported in this paper.

#### Data availability

Data will be made available on request.

#### Acknowledgements

This work was supported by the National Natural Science Foundation of China (22225808, 22075111), Sino-German Cooperation Group Project (GZ1579), Jiangsu Province Innovation Support Program International Science and Technology Cooperation Project (BZ2022045).

#### Appendix A. Supporting information

Supplementary data associated with this article can be found in the online version at [doi:10.1016/j.apcatb.2022.122292](https://doi.org/10.1016/j.apcatb.2022.122292).

#### References

- [1] G. James, Photocatalysis: into the dark, *Nat. Energy* 2 (2017) 16211.
- [2] M.J. Yang, L. Sun, J.F. Huang, D.S. Yu, W. Hong, X.D. Chen, Freestanding graphitic carbon nitride photonic crystals for enhanced photocatalysis, *Adv. Funct. Mater.* 26 (2016) 4943–4950.
- [3] Y.T. Gao, X.D. Xiao, L.P. Zhang, H.G. Fu, A promoted charge separation/transfer system from Cu single atoms and  $C_3N_4$  layers for efficient photocatalysis, *Adv. Mater.* 32 (2020), 2003082.
- [4] B.T. Liu, T. Li, Z.B. Fang, Q. Yin, R. Wang, T.F. Liu, Integrating active  $C_3N_4$  moieties in hydrogen-bonded organic frameworks for efficient photocatalysis, *J. Mater. Chem. A* 9 (2021) 4687–4691.
- [5] F. Yang, Q.Z. Zhang, S. Zhou, N. Bao, Z.H. Xue, M. Chakera, D.L. Maa, Broadband photocatalysts enabled by 0D/2D heterojunctions of near-infrared quantum dots/graphitic carbon nitride nanosheets, *Appl. Catal. B Environ.* 270 (2020), 118879.
- [6] L.Q. Sun, F. Raziq, Y.Y. Wang, L.Q. Jing, Synthesis of large surface-area  $g-C_3N_4$  comodified with  $MnO_x$  and  $Au-TiO_2$  as efficient visible-light photocatalysts for fuel production, *Adv. Energy Mater.* 8 (2018).
- [7] H. Tian, X. Liu, Z. Liang, P. Qiu, X. Qian, H. Cui, J. Tian, Gold nanorods/ $g-C_3N_4$  heterostructures for plasmon-enhanced photocatalytic  $H_2$  evolution in visible and near-infrared light, *J. Colloid Interface Sci.* 557 (2019) 700–708.
- [8] S. Kim, M.S. Zhu, L. Mao, M. Fujitsuka, J.Y. Zhang, X.C. Wang, T. Majima, Metal-free photocatalyst for  $H_2$  evolution in visible to near-infrared region: black phosphorus/graphitic carbon nitride, *J. Am. Chem. Soc.* 139 (2017) 13234–13242.
- [9] M.F. He, L.Y. Fei, R. Guo, C.L. Feng, Ultrastable metal-free near-infrared-driven photocatalysts for  $H_2$  production based on protonated 2D  $g-C_3N_4$  sensitized with Chlorin e6, *Appl. Catal. B Environ.* 260 (2020), 118137.
- [10] S.F. Kang, Y.F. Liu, L.F. Cui, Z. Ma, Boosting near-infrared-driven photocatalytic  $H_2$  evolution using protoporphyrin-sensitized  $g-C_3N_4$ , *J. Photochem. Photobiol. A Chem.* 396 (2020), 112517.



- [11] Y.X. Ding, N. Li, X. Tao, Efficient, full spectrum-driven  $H_2$  evolution Z-scheme  $Co_2P/CdS$  photocatalysts with Co-S bonds, *ACS Appl. Mater. Interfaces* 11 (2019) 22297–22306.
- [12] Y. Gao, W.C. Huang, J.X. Wang, W.W. Cao, Plasmonic enhanced reactive oxygen species activation on low-work-function tungsten nitride for direct near-infrared driven photocatalysis, *Small* 16 (2020), e2004557.
- [13] H.Y. Tan, Y. Yang, B. Cheng, J. Fan, J.G. Yu, W.K. Ho, Near-infrared-responsive photocatalysts, *Small Methods* 5 (2021), e2001042.
- [14] M.J. Fan, Y.S. Xu, Q.J. He, Homogeneous carbon/potassium-incorporation strategy for synthesizing red polymeric carbon nitride capable of near-infrared photocatalytic  $H_2$  production, *Adv. Mater.* 33 (2021), e2101455.
- [15] B. Tian, W. Gao, W.Y. Zhang, X.Q. Zhang, Y.Q. Wu, G.X. Lu, NIR light driven catalytic hydrogen generation over semiconductor photocatalyst coupling up-conversion component, *Appl. Catal. B Environ.* 257 (2019), 117908.
- [16] C. Yu, J.W. Chang, X.D. Song, X.Y. Tan, Y.W. Ding, Z.B. Zhao, J.S. Qiu, A C-S-C linkage-triggered ultrahigh nitrogen-doped carbon and identification of active site in triiodide reduction, *Angew. Chem. Int. Ed.* 133 (2020) 3631–3639.
- [17] Y. Hu, W. Li, E.R. Castellón, T.J. Bandoz, Alterations in the surface features of S-doped carbon and g- $C_3N_4$  photocatalysts in the presence of  $CO_2$  and water upon visible light exposure, *J. Mater. Chem. A* 5 (2017) 16315–16325.
- [18] S. Los, M. Seredych, D.A. Giannakoudakis, E.R. Castellon, T.J. Bandoz, Photoactivity of g- $C_3N_4$ /S-doped porous carbon composite: synergistic effect of composite formation, *ChemSusChem* 9 (2016) 795–799.
- [19] Y.Z. Hong, L.Y. Wang, E.L. Liu, X.X. Duan, X. Lin, J.Y. Shi, A bottom-up acidification strategy engineered ultrathin g- $C_3N_4$  nanosheets towards boosting photocatalytic hydrogen evolution, *Carbon* 163 (2020) 234–243.
- [20] D. Li, Y.Y. Huang, Z.Y. Fang, W.D. Shi, Controlling carbon self-doping site of g- $C_3N_4$  for highly enhanced visiblelight-driven hydrogen evolution, *Appl. Catal. B Environ.* 254 (2019) 128–134.
- [21] B. Wang, Q. Han, J. Gao, L.T. Qu, Atomically thin mesoporous nanomesh of graphitic  $C_3N_4$  for high-efficiency photocatalytic hydrogen evolution, *ACS Nano* 10 (2016) 2745–2751.
- [22] K. Maeda, X.C. Wang, A. Thomas, K. Takanabe, G. Xin, J.M. Carlsson, K. Domen, M. Antonietti, A metal-free polymeric photocatalyst for hydrogen production from water under visible light, *Nat. Mater.* 8 (2009) 76–80.
- [23] H.B. Yang, H.B. Tao, J.Z. Chen, J.W. Miao, B. Liu, Biomolecule-assisted synthesis of carbon nitride and sulfur-doped carbon nitride heterojunction nanosheets: an efficient heterojunction photocatalyst for photoelectrochemical applications, *Beilstein J. Nanotechnol.* 5 (2014) 770–777.
- [24] X.W. Jiang, Z.I. Wang, M. Pan, Y.M. Shi, Nano-scale pore structure and its multi-fractal characteristics of tight sandstone by  $N_2$  adsorption/desorption analyses: a case study of shihezi formation from the sulige gas field, Ordos Basin, China, *Minerals* 10 (2020).
- [25] T.J. Zhao, B. Zhang, W.J. Feng, Y.X. Liu, H.H. Wang, H. Su, L.B. Lv, X.H. Li, J. S. Chen, Polarized few-layer g- $C_3N_4$  as metal-free electrocatalyst for highly efficient reduction of  $CO_2$ , *Nano Res.* 11 (2018) 2450–2459.
- [26] R.R. Wang, P.J. Yang, M. Zhou, X.C. Wang, Photochemical construction of carbonitride structures for red-light redox catalysis, *Angew. Chem. Int. Ed.* 57 (2018) 8674–8677.
- [27] Q. Lia, K. Wang, B.S. Liua, B. Chenga, W. Hob, J.G. Yu, Sulfur-doped g- $C_3N_4$  with enhanced photocatalytic  $CO_2$ -reduction performance, *Appl. Catal. B Environ.* 177 (2015) 44–52.
- [28] W.H. Lv, H. Qin, J.H. Tang, J.R. Bai, Q.F. Zhou, Sulfur-doped porous graphitic carbon nitride heterojunction hybrids for enhanced photocatalytic  $H_2$  evolution, *J. Mater. Sci.* 54 (2018) 4811–4820.
- [29] Z.H. Hong, J.L. Chen, Y.L. Chen, B.Z. Lin, B.F. Gao, One-step synthesis of sulfur-doped and nitrogen-deficient g- $C_3N_4$  photocatalyst for enhanced hydrogen evolution under visible light, *Mater. Lett.* 145 (2015) 129–132.
- [30] X.Q. Bai, W.C. Wang, Q. Ci, L.L. Du, X.G. Ren, D.L. Phillips, Near-field drives long-lived shallow trapping of polymeric  $C_3N_4$  for efficient photocatalytic hydrogen evolution, *Adv. Funct. Mater.* 31 (2021).
- [31] Y.R. Liu, X. Zhou, Z.Y. Jin, M.N. Huang, W.Y. Wong, Solar-driven hydrogen generation catalyzed by g- $C_3N_4$  with poly(platinaynes) as efficient electron donor at low platinum content, *Adv. Sci.* 8 (2021), 2002465.
- [32] J.G. Yu, D.Y. Kim, Boron doping induced charge transfer switching of a  $C_3N_4/ZnO$  photocatalyst from Z-scheme to type II to enhance photocatalytic hydrogen production, *Appl. Catal. B Environ.* 282 (2021), 119538.
- [33] J.G. Yu, X. Li, J.X. Low, Y.P. Fang, J. Xiao, X.B. Chen, Engineering heterogeneous semiconductors for solar water splitting, *J. Mater. Chem. A* 3 (2015) 2485–2534.
- [34] S.Y. Xie, J.H. Liu, Z.B. Geng, K.K. Huang, L. Fan, W.L. Zhou, L.X. Qiu, D.L. Gao, L. Ji, L. Duan, L.H. Lu, W.F. Li, S.Z. Bai, Z.R. Liu, W. Chen, S.H. Feng, Y.G. Zhang, Carbon nitride supramolecular hybrid material enabled high-efficiency photocatalytic water treatments, *Nano Lett.* 16 (2016) 6568–6575.
- [35] H.C. Lee, C. Bhattachary, A.J. Bar, Rapid screening by scanning electrochemical microscopy (SECM) of dopants for  $Bi_2WO_6$  improved photocatalytic water oxidation with Zn doping, *J. Phys. Chem. C* 117 (2013) 9633–9640.
- [36] Y.C. Zhen, Z.S. Hong, Y.R. Ruan, M.D. Wei, Rational design and general synthesis of S-doped hard carbon with tunable doping sites toward excellent Na-ion storage performance, *Adv. Mater.* 30 (2018), 1802035.
- [37] C.Y. Chen, J. Cui, W.K. H, J. Avila, L.D. Zhao, M.C. Asensio, J.Q. Heb, Y. Chen, Large enhancement of electrical transport properties of SnS in the out-of-plane direction by n-type doping: a combined ARPES and DFT study, *J. Mater. Chem. A* 6 (2018) 24588–24594.
- [38] Y. Xu, W.G. Tu, J.J. Wang, B.W. Zhang, M. Kraft, R. Xu, Investigating the role of tunable nitrogen vacancies in graphitic carbon nitride nanosheets for efficient visible-light-driven  $H_2$  evolution and  $CO_2$  reduction, *ACS Sustain. Chem. Eng.* 5 (2017) 7260–7268.
- [39] F. Urbach, The long-wavelength edge of photographic sensitivity and of the electronic absorption of solids, *Phys. Rev.* 92 (1953), 1324–1324.
- [40] X.Y. Kong, J.Y. Tang, B.J. Ng, Y.H. Chew, A.R. Mohamed, S.P. Chai, Midgap-state-mediated two-step photoexcitation in nitrogen defect-modified g- $C_3N_4$  atomic layers for superior photocatalytic  $CO_2$  reduction, *Catal. Sci. Technol.* 9 (2019) 2335–2343.